Geophysical Journal International

Geophys. J. Int. (2024) **239,** 1775–1788
Advance Access publication 2024 September 30
GJI Seismology

https://doi.org/10.1093/gji/ggae350

2-D sedimentary structures at the southeast margin of the Tarim Basin, China, constrained by Love wave ambient noise tomography

Tongtong Xie,[1,2] Yingjie Yang [1] Tao Xu,[2,3] Xiaobo Tian,[3,4] Jiyan Lin,[5] Chenglong Wu[2,3] and Zhanwu Lu[6]

[1] *Department of Earth and Space Sciences, Southern University of Science and Technology, Shenzhen* 518055*, China. E-mail:yangyj@sustech.edu.cn*
[2] *Key Laboratory of Mineral Resources, Institute of Geology and Geophysics, Chinese Academy of Sciences, Beijing* 100029*, China. E-mail: xutao@mail.iggcas.ac.cn*
[3] *Innovation Academy for Earth Science, CAS, Beijing* 100029*, China*
[4] *State Key Laboratory of Lithospheric Evolution, Institute of Geology and Geophysics, Chinese Academy of Sciences, Beijing* 100029*, China*
[5] *Geophysical Exploration Center, China Earthquake Administration, Zhengzhou* 450002*, China*
[6] *Institute of Geology, Chinese Academy of Geological Sciences, Beijing* 100037*, China*

Accepted 2024 September 18. Received 2024 September 12; in original form 2024 January 12

SUMMARY

Imaging the detailed structure of sedimentary basins is crucial for natural resource exploration and essential for better analysis and correction of sediment responses when studying deeper interior earth structures using seismic data. In the Tarim Basin, previous studies on the sedimentary structures are mostly obtained by active-source seismic surveys, which can provide high-resolution underground interface information but are highly costly or environmentally unfriendly. In this paper, ambient noise tomography, an efficient and economical method based on background vibration, is employed to construct the sedimentary velocity structure at the southeast margin of the Tarim Basin. Based on ambient noise data collected from a linear dense short-period seismic array, we extract Love wave signals from *T–T* component cross-correlation functions (CCFs) and measure Love wave dispersion curves at a period band of ∼0.3–11.5 s. Then, we utilize a one-step direct surface wave tomography method to image a fine 2-D sedimentary shear wave velocity structure with a depth reaching 10 km. Our results reveal a clear layered sedimentary structure, the palaeo Tadong uplift and the thrust Cherchen fault. Our study provides reference sedimentary velocity models for the southeastern Tarim Basin, focusing on depths shallower than 10 km. This model is intended to serve as crucial input for studies requiring detailed shallow sedimentary velocity data. Moreover, our research demonstrates that the application of the ambient noise tomography method with dense arrays has great potential for enhancing resource exploration efforts in sedimentary basins.

Key words: Crustal imaging; Empirical Green's function; Seismic interferometry; Seismic noise; Seismic tomography.

1. INTRODUCTION

The Tarim Basin, situated in the northwest of China, is the largest inland basin in China. It has undergone long and intricate tectonic evolution from the Sinian to the Quaternary. This has led to the formation of a large-scale superimposed basin abundant in oil and natural gas resources (Huang *et al.* 2017; Kang 2018; Yang *et al.* 2021). The distribution of these energy resources within the basin is highly related to the structure of fault belts, superimposed unconformities, depressions, palaeo-uplift belts and slopes (Lin *et al.* 2012a;b; Tang *et al.* 2014; Liu *et al.* 2016; Kang 2018; Ren *et al.* 2018; Tian *et al.* 2021; Yang *et al.* 2021). Research on the sedimentary structure of the Tarim Basin holds great significance for comprehending the evolution and facilitating the field exploration of hydrocarbon resources.

In recent decades, numerous active-source seismic studies have been conducted to examine the fine structure of the Tarim Basin for hydrocarbon resource exploration. Utilizing seismic structural and stratigraphic interpretation profiles, high-resolution sedimentary structures have been deduced through the analysis of local onlap reflection characteristics (Liu *et al.* 2016). However, the deployment of 2-D/3-D active seismic experiments is considered either environmentally unfriendly due to the use of explosives or economically costly when using vibroseis trucks and other active sources.

More recently, the ambient noise tomography method, based on background vibrations, has proven to be an efficient and reliable

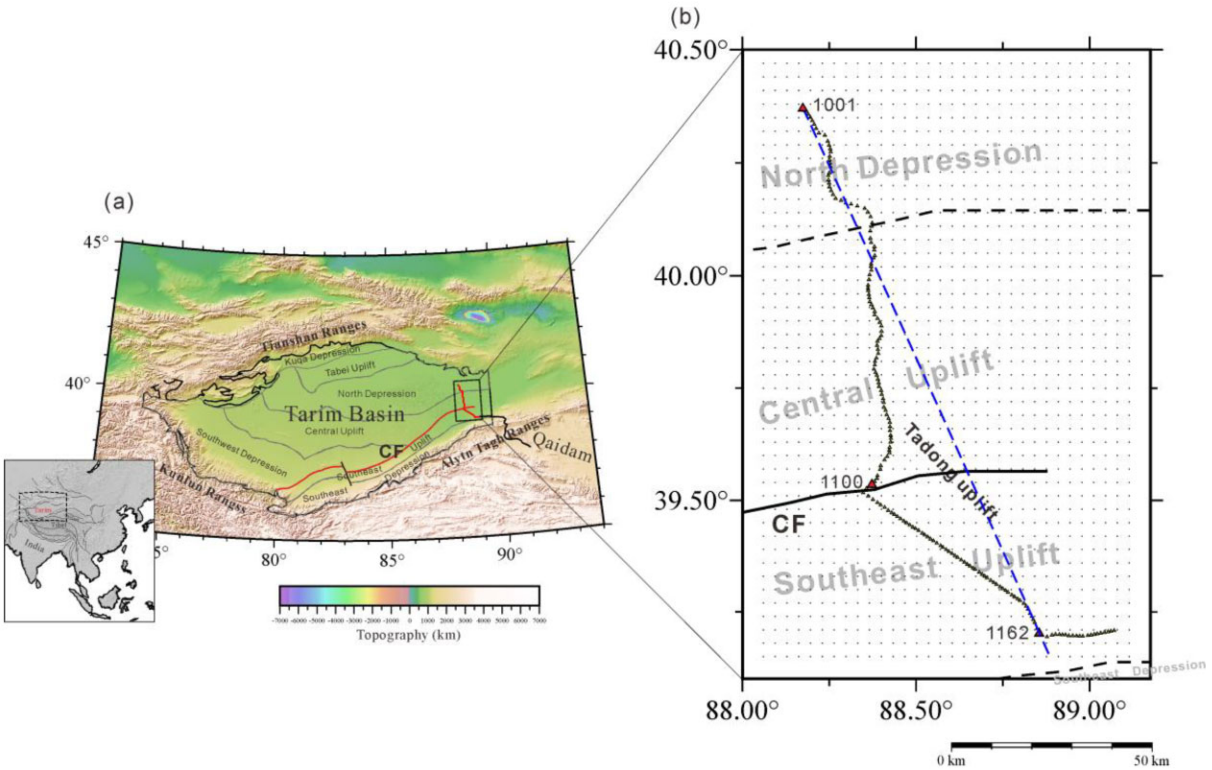

Figure 1. (a) Geological map of the Tarim Basin. The bottom-left insert shows the location of the Tarim Basin (denoted in a black dashed rectangle) and its surrounding tectonic units in a larger scale. In the main figure, the black solid rectangle outlines our study areas. The CF, depicted as a solid red line, crosses our study area. (b) The distribution of the NTB subarray used in this study. The red triangle represents stations 1001, 1100 and 1162, respectively, from the north to the south. The blue dashed line from station 1001 to 1162 indicates the profile to which our V_{sh} profile (plotted in Fig. 12) is projected. The small grey dots represent the grid that parametrizes the study area in the longitude and latitude directions in the inversion. The distributions of the boundaries of the tectonic units (grey lines) in the Tarim Basin, the CF and the Tadong uplift are all obtained from Liu *et al.* (2016).

approach to image shear wave velocity (*Vs*) structure of the interior of the earth (e.g. Sabra *et al.* 2005; Yao *et al.* 2006; Yang *et al.* 2007; Lin *et al.* 2008, 2014; Rivet *et al.* 2015; Li *et al.* 2016; Wang *et al.* 2019a; Jiang & Denolle 2022). In the Tarim Basin, previous ambient noise studies have primarily concentrated on imaging the deep crustal and upper-mantle structure through the inversion of surface wave dispersion curves at periods longer than ∼5 s (e.g. Yang *et al.* 2010; Li *et al.* 2012; Lü *et al.* 2019; Sun *et al.* 2022; Tan *et al.* 2023). However, the shallow sedimentary velocity structure in the Tarim Basin is rarely imaged despite its importance in petroleum exploration and mitigating sedimentary reverberations in seismic recordings (Li *et al.* 2019).

With the technological advancement of portable short-period seismometers and the reduced cost and streamlined operation of these instruments, it is highly feasible and cost-effective to deploy dense short-period seismic arrays. The utilization of passive source short-period dense arrays has undergone rapid development for imaging shallow crustal structures. It can serve as a foundation for imaging sedimentary structures, as evidenced by various studies (e.g. Lin *et al.* 2013; Bao *et al.* 2018; Tomar *et al.* 2018; Chmiel *et al.* 2019; Wang *et al.* 2019b).

In this study, we combine the advantages of the ambient noise tomography method and the dense short-period array to image fine sedimentary velocity structures at the southeast margin of the Tarim Basin. We utilize Love wave signals in the *T*–*T* component CCFs and adopt a one-step surface wave direct solution method to obtain the shallow sedimentary velocity structure. By comparing our inversion results with previous studies, such as active source seismic profiles, we demonstrate that ambient noise tomography based on short-period dense arrays is promising for imaging sedimentary structures in resource explorations.

2. GEOLOGICAL SETTINGS

The Tarim Basin, the largest inland basin in China, is approximately 1500 km long and 700 km wide (Laborde *et al.* 2019). Bounded by the Kunlun Ranges in the west, the Tianshan Ranges in the north and the Alyth Tagh Range in the southeast, the Tarim Basin plays an integral part in the Cenozoic Asian orogenic system (Zhao *et al.* 2006).

Having undergone a long-term tectonic geological evolution, the Tarim Basin has formed a Proterozoic basement composed of igneous rocks overlain by thick sedimentary layers from the Sinian to the Quaternary (Lin *et al.* 2012b; Liu *et al.* 2016; Laborde *et al.* 2019). Seven main tectonic units are distributed in the Tarim Basin, including four depressions and three uplifts: the Southwest Depression, the North Depression, the Kuqa Depression, the Southeast Depression, the Tabei uplift, the Central uplift and the Southeast uplift (Liu *et al.* 2012, 2016; Lin *et al.* 2012a, b). Our research area encompasses the southeast margin of the Tarim Basin, traversing through distinct geological features, including the North Depression, the Central uplift, the Southeast uplift and the Southeast Depression from north to south, bordered by the Altyn Fault Zone. Within the region of the Southeast Depression, both the basement and sedimentary cover of the Tarim Basin are slightly

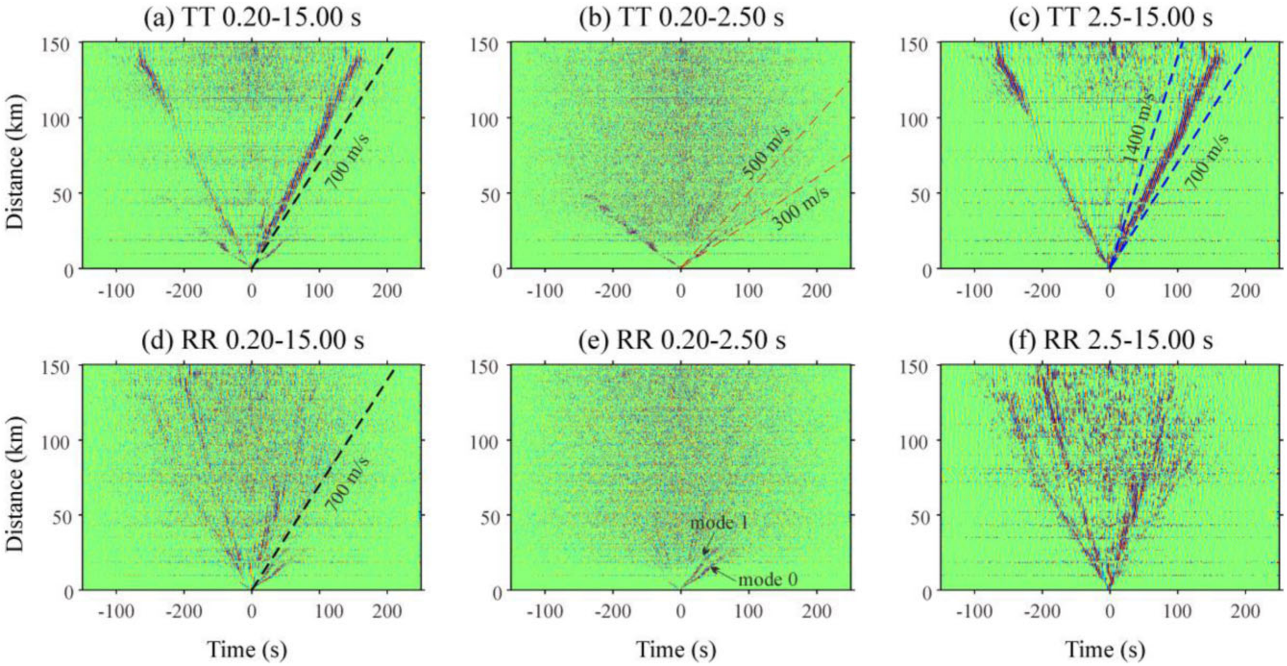

Figure 2. A record section of (a)–(c) *T*–*T* and (d)–(f) *R*–*R* component CCFs between station 1001 (marked in Fig. 1) and all the other stations. The *TT* component CCFs are filtered at period bands of (a) 0.2–15.0, (b) 0.2–2.5 and (c) 2.5–15.0 s, respectively. The *RR* component CCFs are filtered at period bands of (d) 0.2–15.0, (e) 0.2–2.5 and (f) 2.5–15.0 s, respectively. Each CCF is normalized with the maximum value of the waveform. In (a) and (d), the moveout velocities of 700 m s^{-1} are denoted as black dashed lines. In (b), the moveout velocities of ∼300–500 m s^{-1} are denoted as red dashed lines. In (c), the moveout velocities of ∼700–1400 m s^{-1} are denoted as blue dashed lines. In (e), the fundamental and the first higher mode Rayleigh waves are visible, of which the same signals are reported in Xie *et al.* (2023b) and shown in Fig. S1 (Supporting Information).

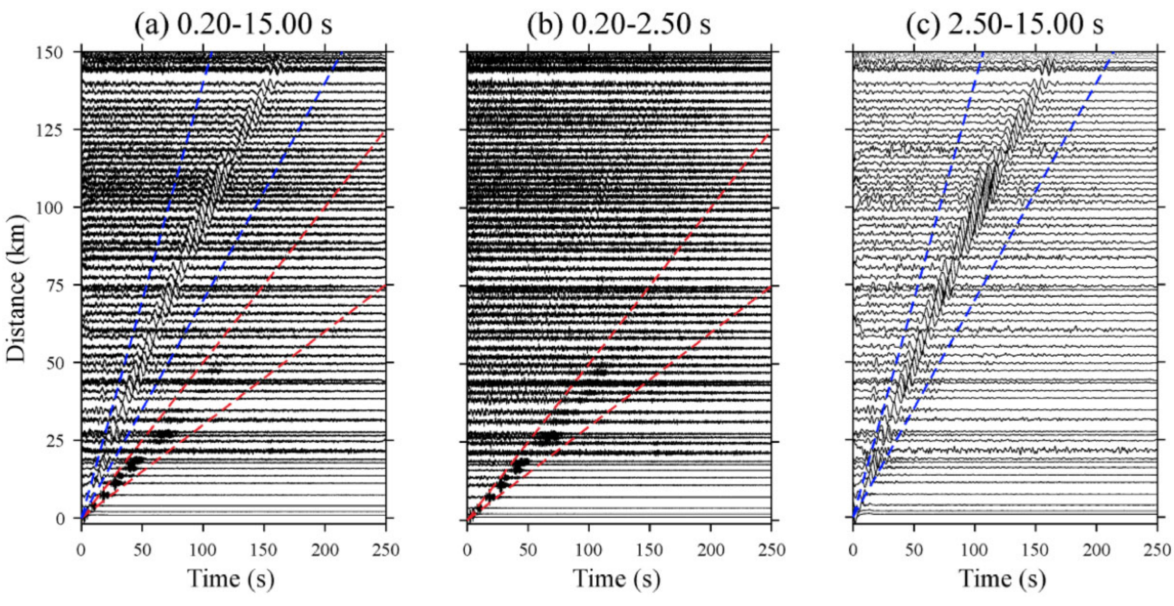

Figure 3. Waveforms of symmetric *T*–*T* component CCFs between station 1001 (marked in Fig. 1) and the other stations. The CCFs are filtered at period bands of (a) 0.2–15.0, (b) 0.2–2.5 and (c) 2.5–15.0 s, respectively. The moveout velocities of ∼300–500 and ∼700–1400 m s^{-1} are denoted as red and blue dashed lines, respectively.

tilted towards the southeast. The Cenozoic sediments in the front of the Altun fault zone are slightly thicker than those in the northwest, with an overall thickness of less than 3 km (Laborde *et al.* 2019).

Additionally, the fault systems present characteristics of multilevel differential development and distribution within the Tarim Basin (Tang *et al.* 2014). A significant fault belt, the Cherchen fault (CF), extends across our study region. The entire CF is a large-scale NE-trending thrust fault belt (red solid line in Fig. 1a) that developed in the basement of the Tarim Basin. It governs the distribution of primary geological units in the basin, as elucidated by Tang *et al.* (2014). It is the main boundary fault on the northern edge of the Southeast uplift and plays a pivotal role in the formation and evolution history of the Southeast uplift (Xu *et al.* 2009; Tang

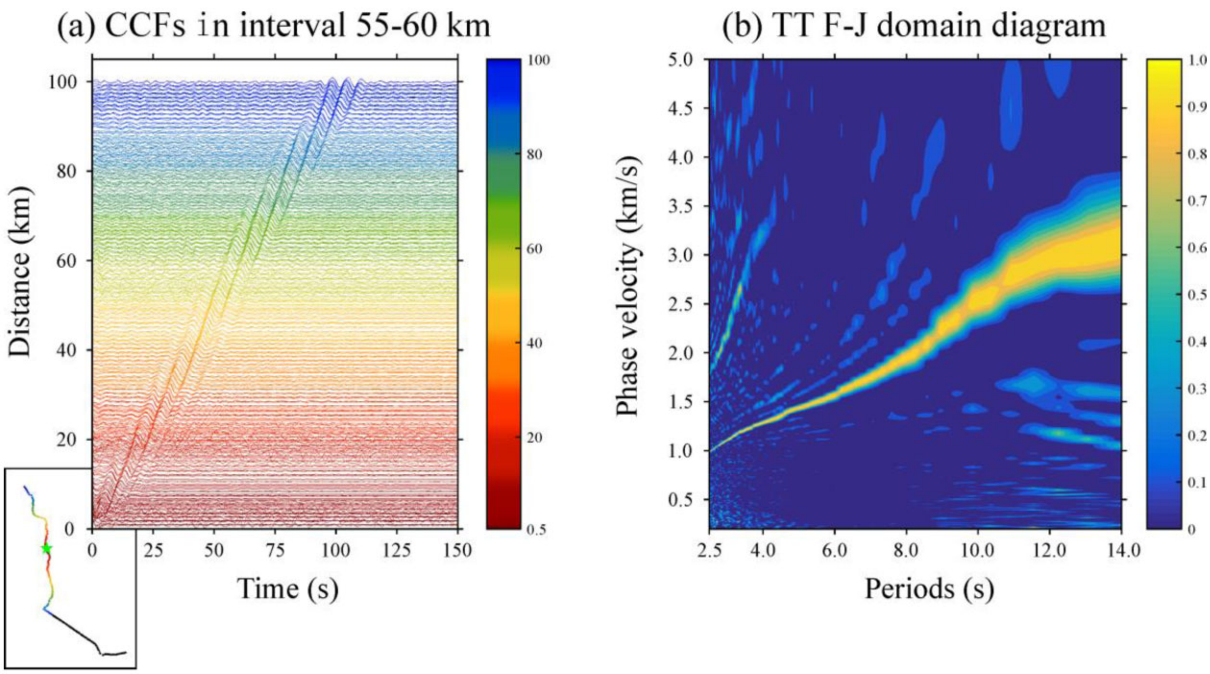

Figure 4. An example of averaged dispersion curves obtained by the F-J method. (a) Waveforms of *T–T* component CCFs with the central points (the green star in the bottom insert) located at the segment interval of 055–060 km. These CCFs are filtered at a period band of 2.5–15 s with a maximum interstation distance of less than 100 km. The station locations of all the *T–T* component CCFs plotted in (a) are shown in the bottom insert. Only those CCFs from the coloured stations are plotted in this figure; colours represent the interstation distances of the CCFs centred at the green star. (b) The F-J diagrams of Love wave dispersion curves based on all the CCFs presented in (a). Colours represent coherence values from 0 (blue) to 1 (yellow).

et al. 2014). The eastern part of the CF is believed to cut across the basement of the Tarim Basin but remains largely hidden under the sedimentary unconformities (Xu *et al.* 2009).

3. PROCESSING OF NOISE DATA

The seismic ambient noise data are collected from a northern part of a dense short-period linear array in the Tarim Basin deployed by the Institute of Geology and Geophysics, Chinese Academy of Sciences (Xie *et al.* 2023b; Wu *et al.* 2024; Yao *et al.* 2024), which is referred to as Northern Tarim Basin (NTB) seismic array (Fig. 1). The NTB subarray, situated in the NTB with thick sedimentary covers, consists of 181 three-component EPS-2-M6Q-C-E20 seismometers. These seismometers have a flat amplitude response over a range of 100 Hz–20 s. The deployment duration spanned from 2021 September 17 to November 20, with an average station spacing of ∼1 km.

In our previous ambient noise study (Xie *et al.* 2023b), we calculated the *Z–Z* component CCFs (Fig. S1, Supporting Information), but were able to retrieve high-quality fundamental and first higher mode Rayleigh wave signals only at periods shorter than 1.9 s. This restricted our imaging capability to depths of approximately 1.24 km or less. In this study, we can extract Love wave signals at a more extended period band of ∼ 0.3–11.5 s between individual station pairs from *T–T* component CCFs to extend our imaging depth.

We follow the data processing procedures of Lin *et al.* (2008) to obtain the *R–R* and *T–T* component CCFs from ambient noise data. With the raw E and N component seismic recordings, we first decimate the raw data from 100 to 20 Hz and cut continuous noise data into hourly segments. Then, we demean and detrend all the hourly segments and remove instrument responses. We then filter the hourly segments at a period band of 0.125–50 s and apply the running-absolute-mean normalization and spectral whitening to the filtered segments (Bensen *et al.* 2007; Lin *et al.* 2014). Afterward, we cross-correlate the hourly E and N component segments between each station pair to obtain the hourly E-E, E-N, N-N and N-E component CCFs. We then linearly stack all the hourly CCFs to obtain the stacked CCFs.

Finally, following the rotation operator in Lin *et al.* (2008),

$$\begin{pmatrix} TT \\ RR \\ TR \\ RT \end{pmatrix} = \begin{pmatrix} -\cos\theta\cos\psi & \cos\theta\sin\psi & -\sin\theta\sin\psi & \sin\theta\cos\psi \\ -\sin\theta\sin\psi & -\sin\theta\cos\psi & -\cos\theta\cos\psi & -\cos\theta\sin\psi \\ -\cos\theta\sin\psi & -\cos\theta\cos\psi & \sin\theta\cos\psi & \sin\theta\sin\psi \\ -\sin\theta\cos\psi & \sin\theta\sin\psi & \cos\theta\sin\psi & -\cos\theta\cos\psi \end{pmatrix} \times \begin{pmatrix} \mathrm{EE} \\ \mathrm{EN} \\ \mathrm{NN} \\ \mathrm{NE} \end{pmatrix} \quad (1)$$

we rotate the E-E, E-N, N-N and N-E CCF to obtain the *T–T*, *T–R*, *R–T* and *R–R* CCFs between each station pair using coefficients associated with the interstation azimuth angle (θ) and backazimuth angle (ψ).

4. *T–T* AND *R–R* CCFs

The *T–T* and *R–R* component CCFs exhibit the Love and Rayleigh wave arrivals, respectively. To analyse the wavefield characteristics in the CCFs, we present a record section of *T–T* and *R–R* component CCFs between station 1001 and all the other stations in Fig. 2, where station 1001 is located at the northmost end of the NTB subarray. These CCFs are bandpass filtered at three-period bands of 0.2–15.0, 0.2–2.5 and 2.5–15.0 s, respectively. We discuss the characteristics of *T–T* and *R–R* component CCFs as follows.

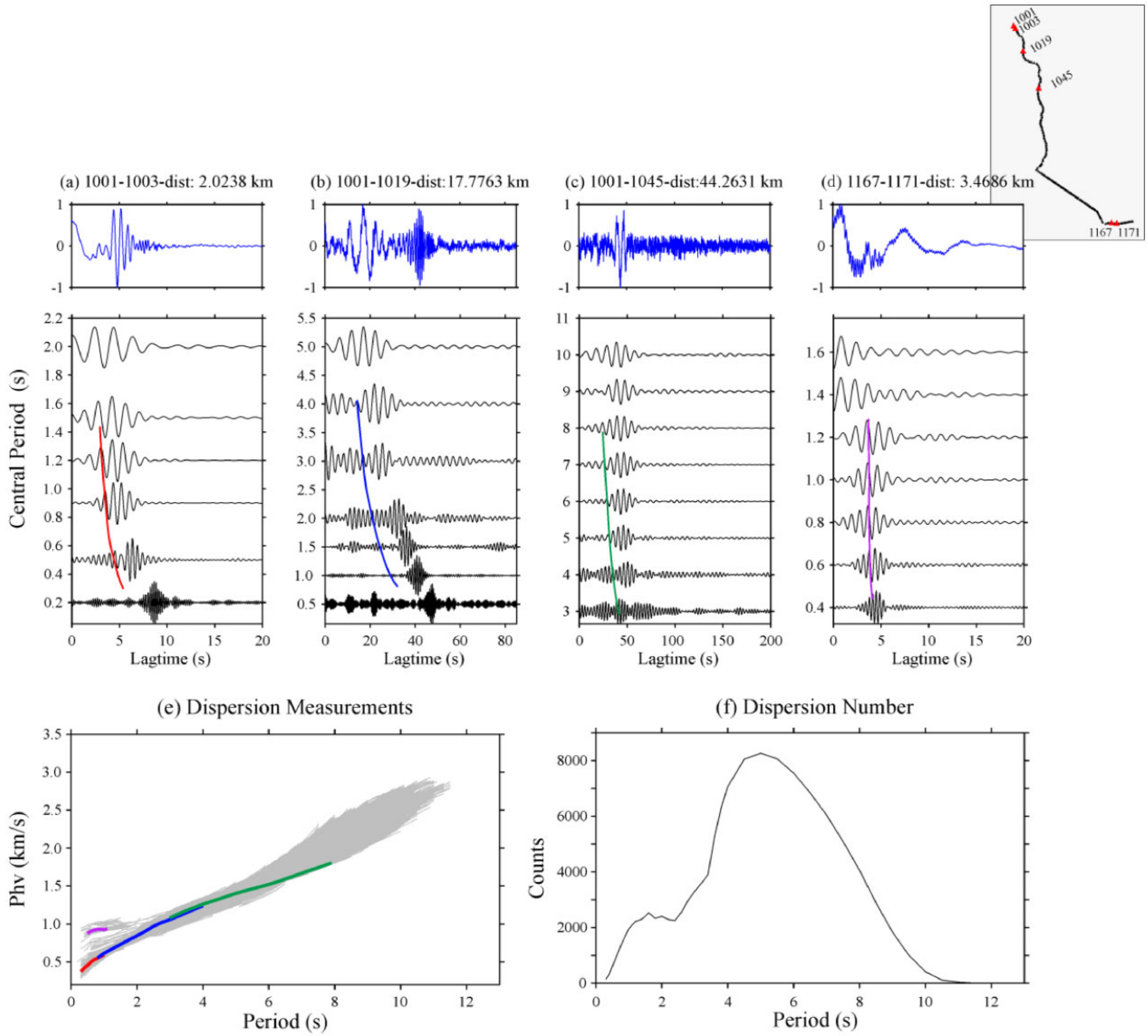

Figure 5. Measurements of Love wave dispersion curves. (a)–(d) Examples of dispersion features of Love waves of four *T*–*T* CCFs. Station locations are plotted in the top right insert. Station pairs and interstation distances are denoted at the top of each diagram (a)–(d). The *T*–*T* CCFs (blue solid lines at the top panels) are narrow bandpass filtered, and the resulting waveforms are plotted in each diagram according to their central filter periods. The reference traveltimes for Love wave signals varying with the period are shown in red, blue, green and purple solid lines. (e) All the Love wave phase velocity dispersion curves measured from *T*–*T* component CCFs between individual station pairs. The dispersion curves of CCFs in (a)–(d) are plotted in red, blue, green and purple solid lines, respectively. (f) The numbers of dispersion measurements at period bands of 0.3–11.5 s.

First, for both the *T*–*T* and *R*–*R* CCFs, the wave trains at the short-period band (∼ 0.2–2.5 s, Figs 2b and e) travel much slower (less than ∼700 m s^{-1}) than those at the long-period band (∼ 2.5–15 s, Figs 2c and f), leading to the distinct separation of wave trains with different moveout velocities between the two different period bands (Figs 2a and d). This is mainly due to that the shallowest sediments are characterized by very low velocities, and with the increasing depths, the seismic velocities increase from the shallowest sedimentary layers to the underlying basement (Corela *et al.* 2017; Jiang & Denolle 2022). This kind of significant velocity contrast can be featured by the high dispersion of surface waves and the separation of wave trains between the short- (relative to the shallowest sediments) and long-period bands (relative to the underlying basement) (Viens *et al.* 2016).

Secondly, the energy of Love wave signals in the *T*–*T* component CCFs are strong and distinct (Figs 2a–c). The Love wave signals present lower group velocities of ∼300–500 m s^{-1} at the period band of 0.2–2.50 s and higher velocities of ∼700–1400 m s^{-1} (Fig. 2b) at the long-period band of 2.5–15.0 s (Fig. 2c).

Thirdly, compared to the Love wave signals, the Rayleigh waves in the *R*–*R* component CCFs are more complex, with higher mode Rayleigh waves also appearing. At the short-period bands of 0.20–2.50 s (Fig. 2e), we observe two groups of wave trains with different moveout velocities. As the *R*–*R* and *Z*–*Z* component CCFs both contain Rayleigh wave signals and we have observed and confirmed the presence of the first higher mode Rayleigh waves in the *Z*–*Z* component CCFs at the same period band of ∼ 0.20–2.0 s in our previous work in Xie *et al.* (2023b), we here can state that the two groups of wave trains with different moveout velocities represent the fundamental and the first higher mode Rayleigh waves, respectively.

At the long-period bands of 2.5–15.0 s for *R*–*R* component CCFs (Fig. 2f), more than one branch of wave trains also appears, indicating the presence of the higher mode Rayleigh waves. Meanwhile,

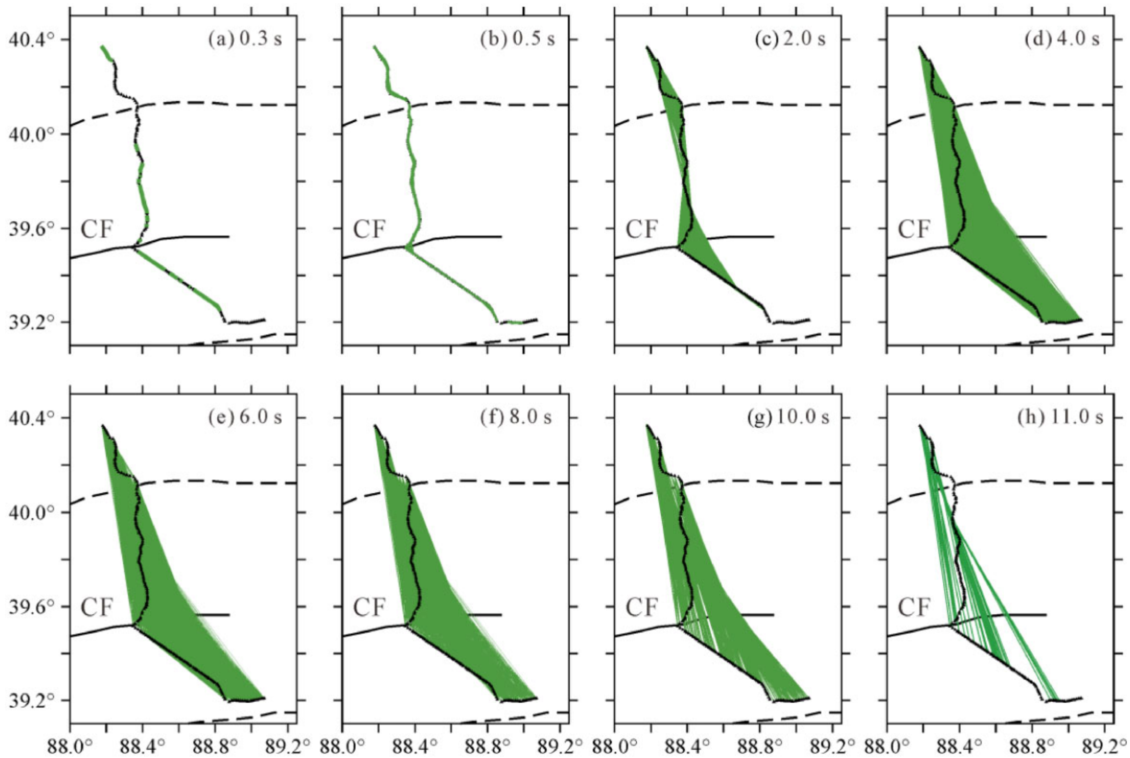

Figure 6. Examples of ray-path coverage at periods of (a) 0.3 s, (b) 0.5 s, (c) 2.0 s, (d) 4.0 s, (e) 6.0 s, (f) 8.0 s, (g) 10.0 s, and (h) 11.0 s, respectively. Please note that the paths for the 0.3 and 0.5 s period diagrams closely follow the linear arrays with minimal distance offset from the station line.

the energy of higher-mode Rayleigh waves is comparable relative to the fundamental modes and interferes with the fundamental mode in the time-domain CCFs. When group velocities of adjacent modes are close to each other, it becomes challenging to identify and separate the different modes in the time domain. In this situation, the traditional frequency–time analysis (FTAN) method (Levshin & Ritzwoller. 2001) is no longer appropriate for dispersion measurements.

Overall, for our data, the energy of fundamental Love wave signals in the *T–T* component CCFs are more pronounced with higher signal-to-noise ratios (SNRs) and not interfered by higher mode signals than Rayleigh waves in *R–R* component CCFs. Therefore, in this study, we only utilize Love wave signals from the *T–T* component CCFs at a period range of ∼0.3–11.5 s to image subsurface structures. For the subsequent dispersion curve measurements, we stack the positive and negative time lags of *T–T* CCFs to have the symmetric *T–T* component of CCFs. Some examples of these symmetric *T–T* component CCFs are shown in Fig. 3.

5. MEASUREMENTS OF LOVE WAVE PHASE VELOCITY DISPERSION CURVES

In phase velocity measurement of surface waves, we need a reference phase velocity dispersion curve to unwrap the phase of surface waves. A useful strategy is to adopt an array-based phase velocity measurement method to obtain an average dispersion curve of a study area as references. Here, we adopt a frequency–Bessel (F-J) method (Wang *et al.* 2019a; Hu *et al.* 2020) to generate a series of average Love wave dispersion curves for references along the seismic array.

To do so, we sort all CCFs according to the location of the midpoint of each CCF path relative to the first station on the northern side of the array. We then group the CCFs into a series of sets with their path midpoints situated in each non-overlapped 5 km bin from the north to the south. For each set of CCFs, we generate F-J diagrams to obtain phase velocity dispersion curves. Fig. 4 shows an example of F-J diagrams of a group of *T–T* CCFs with their path midpoints centred at the segment interval of 55–60 km and a maximum interstation distance of less than 100 km. The central point in the subarray is marked in Fig. 4(a). The corresponding F-J diagrams of *R–R* components are plotted in Fig. S2 (Supporting Information), which display more complex Rayleigh wave dispersion curves and weaker energy at the long-period side of the dispersion image compared to that of *T–T* components.

Utilizing the FTAN method (Levshin & Ritzwoller 2001; Bensen *et al.* 2007), we measure the phase velocity dispersion curves of Love waves between individual station pairs. In the FTAN measurement, for an individual CCF, we use the phase velocities from the F-J diagram of the distance bin, to which the midpoint of this CCF is closest, as the reference phase velocities. Meanwhile, to reduce the systematic deviations of the dispersion data extraction from the horizontal–horizontal CCFs, as presented in Xie *et al.* (2023a), we require the interstation distances of CCFs longer than three wavelengths and SNRs of CCFs larger than five. We define the SNR here using the ratio of the maximum amplitude of Love wave signals to the root mean square (RMS) value within a noise window trailing the Love wave signals in CCFs (Bensen *et al.* 2007; Zhao *et al.* 2020).

We present four examples of dispersion curves extracted from CCFs. Figs 5(a)–(c) again display rapid increases in phase velocities with increasing periods and indicate the strong dispersion features of Love wave propagation. Fig. 5(d) represents higher phase velocities

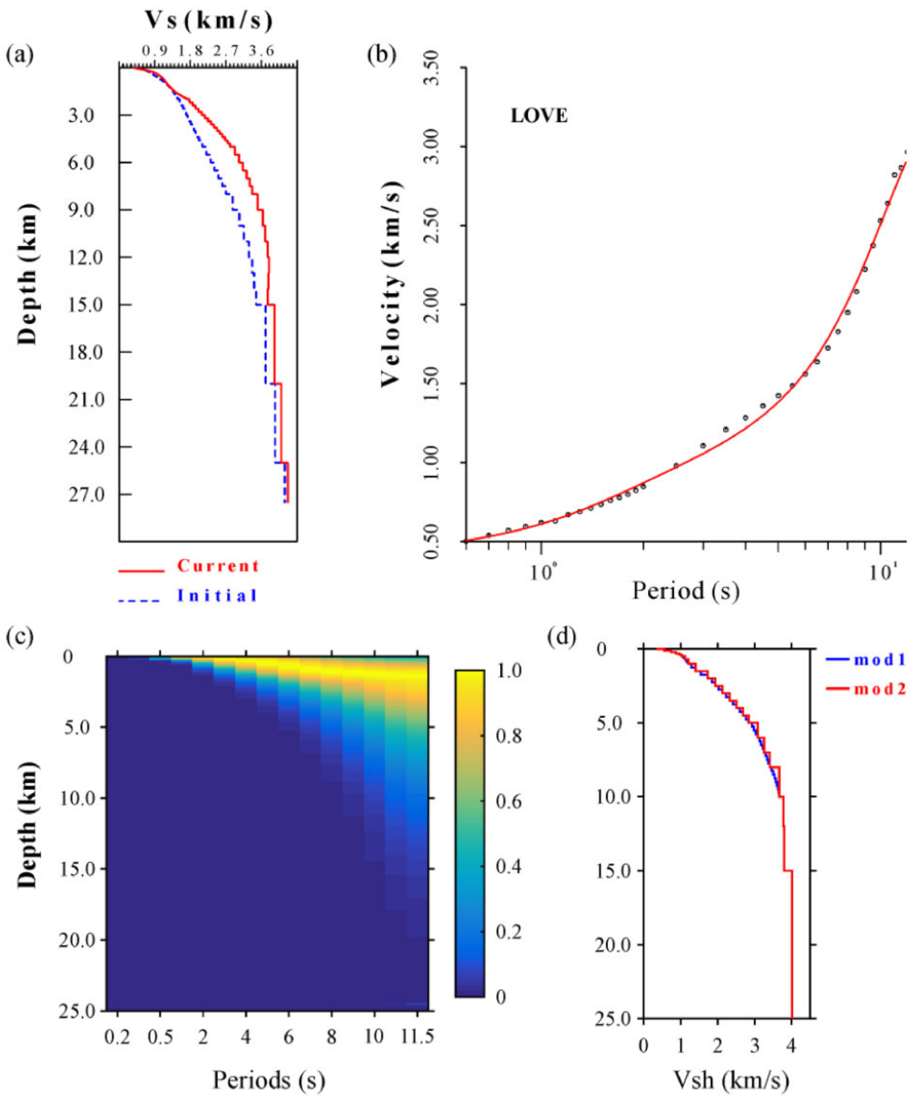

Figure 7. Construction of the 1-D initial model beneath each gridpoint for inversion. (a) The reference input velocity model (in red) obtained by inverting the average dispersion curves in (b) using the CPS program. The initial and inverted velocity models are indicated by the blue dashed and red lines, respectively. The average dispersion curves are obtained using the F-J method. (b) The fitting of Love wave dispersion curves between observations (black points) and synthetics calculated using the inverted model (red line). (c) Normalized sensitivity kernels plotted to show variations with periods and depths, calculated based on the reference input velocity model in (a) using the CPS program. Colours represent normalized sensitivity values from 0 (black) to 1 (yellow). (d) The initial velocity models with two ways of partitioning layer thickness in the vertical direction based on the reference input velocity model. Details of the models are described in the main text.

at the locations approaching the Alyth Tagh Range. The final Love wave dispersion curves used for Love wave tomography are plotted in Fig. 5(e), and the dispersion numbers of different periods are plotted in Fig. 5(f). In addition, we also present examples of ray-path coverage of Love wave dispersion curves at several periods in Fig. 6. The spatial extent of ray-path coverage is overall dense at periods shorter than 10.0 s and sparse at 11.0 s period.

6. DIRECT SURFACE WAVE TOMOGRAPHY

6.1 Method

With the measured interstation phase velocity dispersion data, we adopt a direct surface wave tomography (DSurfTomo) method developed by Fang *et al.* (2015) to image the sedimentary velocity structure. This one-step method avoids the intermediate inversion steps of constructing phase or group velocity maps and considers the ray-bending effects. In this method, the whole study area is parametrized as a 3-D model by a regular grid in both the horizontal and vertical directions. The 3-D velocity model is represented as a stack of 1-D layered shear wave velocity models beneath each location (like each grey dot in Fig. 1b).

In the inversion process, local dispersion curves of surface waves for the 1-D layered velocity model at each location are first forward calculated using the Computer Programs in Seismology (CPS) program (Herrmann 2013). Then, for individual periods, a series of 2-D phase velocity maps are constructed using the point-wise phase velocity dispersion curves. Subsequently, the ray paths of the surface waves between each station pair are traced using a fast-marching method, which considers ray bending, and the predicted traveltimes are calculated (Rawlinson & Sambridge 2005). The variation of

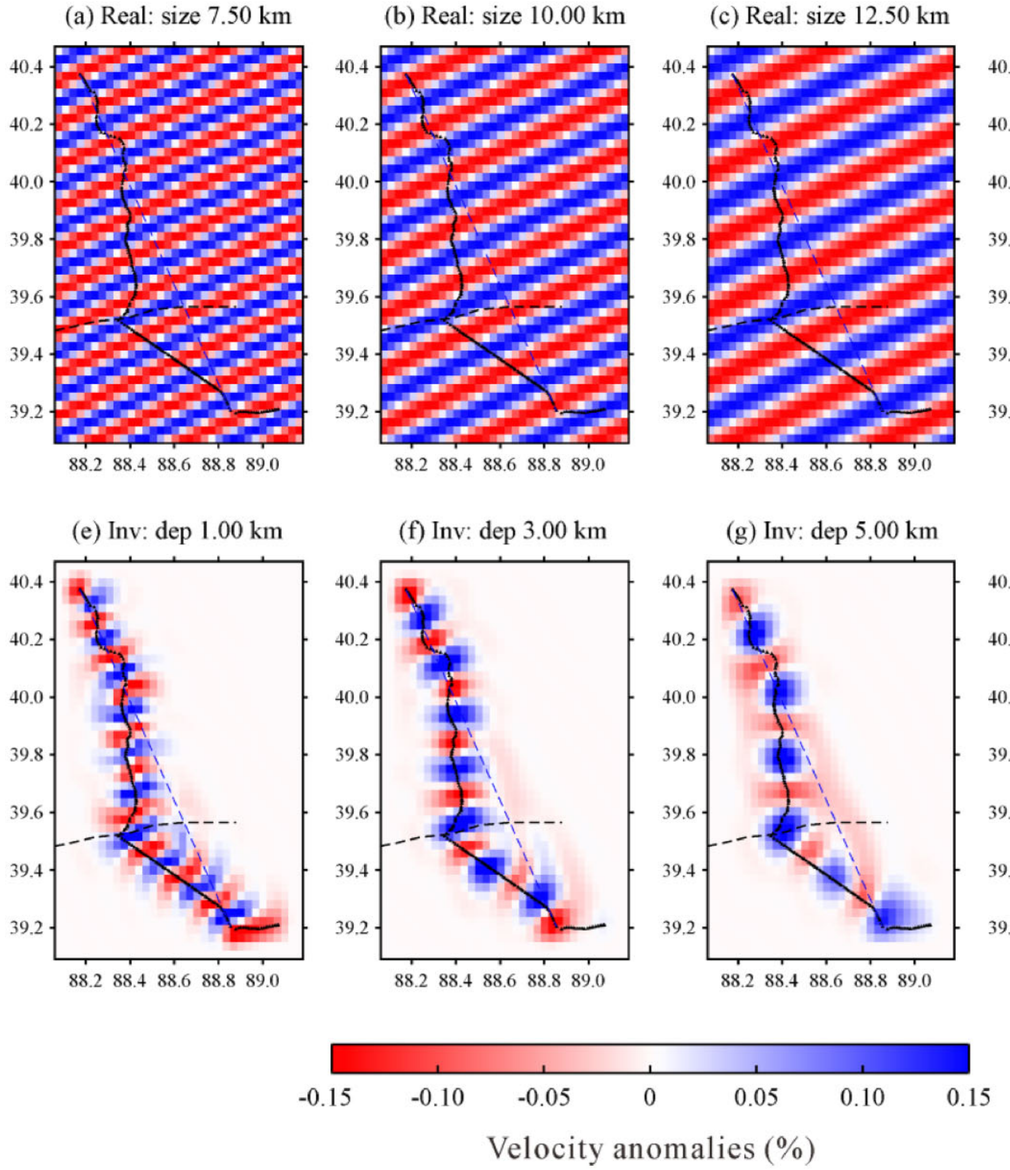

Figure 8. Map view of checkerboard resolution tests along the projection line with grid node sizes of 0.030° × 0.034° in the latitude and longitude directions, respectively. (a)–(d) Input checkerboard models with anomaly sizes of 7.5, 10.0, 12.5 and 15.0 km along the projection line, respectively. (e)–(f) Horizontal slices of recovered checkerboard models with anomaly sizes of 7.5 km at an inversion depth of 1.0 km, 10.0 km at an inversion depth of 3.0 km, 12.5 km at an inversion depth of 5.0 km, and 15.0 km at an inversion depth of 7.0 km, respectively. The blue dashed line represents the projection line, and the black dashed line indicates the CF.

surface wave traveltimes is then linked to the perturbation of the elastic parameters (i.e. the *Vs*) according to eq. 10 of Fang *et al.* (2015). Finally, the shear wave velocity model is iteratively optimized to minimize the traveltime differences between the model predictions and the observations (Fang *et al.* 2015). The objective function Φ(m) is defined as detailed below:

$$\Phi(\mathbf{m}) = ||\mathbf{d} - \mathbf{Gm}||_2^2 + \lambda||\mathbf{Lm}||_2^2. \qquad (2)$$

Here, $||\cdots||_2^2$ is the ℓ_2-norm operator, **d** is the traveltime residual vector including all the ray paths at all periods of surface waves, **G** represents the sensitivity kernel matrix and **m** represents the model vector of shear velocity perturbation, **L** represents a smoothing parameter of models and λ is a weight value balancing the first term of data fitting $||\mathbf{d} - \mathbf{Gm}||_2^2$and second term of model regularization $||\mathbf{Lm}||_2^2$.

In the DSurfTomo method, a reliable reference velocity model is needed to establish the initial model for the inversion process. Considering that the initial 3-D velocity model is represented by stacks of 1-D layered velocity models beneath each location, we first build a reliable 1-D reference layered velocity model (the red solid line in Fig. 7a) by inverting the average dispersion curves (in Figs 4b and 7b) using CPS program (Herrmann 2013). Based on this reference model, we then conduct the following checkerboard resolution test and field data inversion.

6.2 Checkerboard resolution tests

In tomography, a checkerboard resolution test is an effective way to evaluate the resolution of sensitivity of seismic data in imaging underground velocities, which depends on the coverage density of

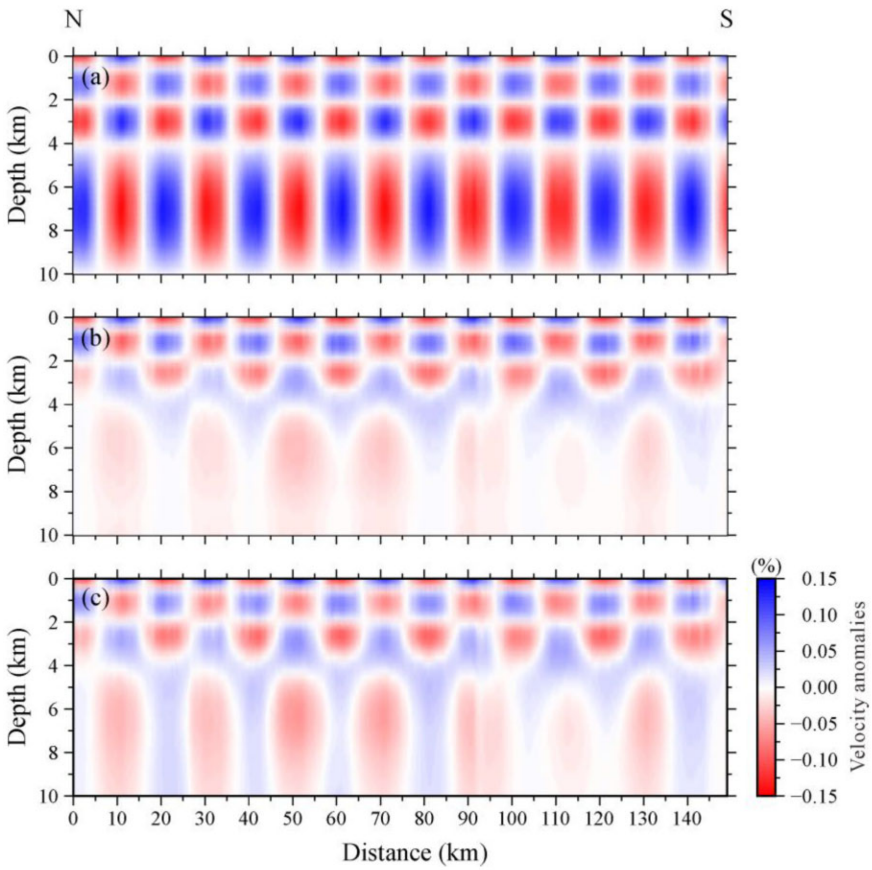

Figure 9. V_{sh} transects of checkerboard resolution tests using two ways of partitioning the layer thickness in the vertical direction. (a) The input checkerboard model with anomaly sizes of 0.5, 1.5, 2.0 and 6.0 km in the depth direction and a fixed 10 km on the horizontal axis. (b) Checkerboard models recovered with relatively uniform thickness (mod1 in Fig. 7d). (c) Checkerboard models recovered with increasing thickness from 0.1 to 2 km from the subsurface down to 10 km (mod2 in Fig. 7d). The grid sizes in the latitude and longitude directions are $0.030^\circ \times 0.034^\circ$, respectively.

the ray paths beneath the array. And the size of grid nodes used for model parametrization can be determined by balancing the relationship between the sizes of grid nodes and recoverable anomaly scales.

For the construction of checkerboard velocity models, the background velocities of the 1-D layered velocity model are obtained based on the reference model shown in Fig. 7(a). The maximum velocity perturbations for the velocity anomalies are set to be $\pm$ 15 per cent of the background velocity. Given our quasi-linear array, we define a projection line (the blue dashed line in Fig. 1b) to visualize inversion results by projecting velocities beneath each station onto this line. For lateral variations in velocities, we design several different anomaly sizes of 7.5, 10.0, 12.5 and 15.0 km along the projection line (Figs 8a–d). Regarding vertical variations, the anomaly sizes increase from 0.5 to 6 km in the depth direction (Fig. 9a).

In setting up grid node sizes for inversion models, we test four different node sizes: $0.015^\circ \times 0.017^\circ$, $0.020^\circ \times 0.020^\circ$, $0.030^\circ \times 0.034^\circ$ and $0.040^\circ \times 0.040^\circ$ in the latitude and longitude directions, respectively. For constructing the 1-D layered velocity model beneath each gridpoint, we also test two ways of partitioning the layer thickness in the vertical direction. According to the normalized sensitivity kernels plotted in Fig. 7(c), the maximum sensitivity depth reaches approximately up to 10 km. Therefore, one model divides layers with relatively uniform thickness, intervals being 0.1 km from 0 to 1.0 km and 0.25 km from 1 to 10 km (mod1 in Fig. 7d). The other model increases layer thickness gradually from 0.1 to 2 km from the subsurface down to 10 km (mod2 in Fig. 7d). In both cases, three deeper layers are added at depths of 10–25 km to stabilize the inversion process.

After comparing the results of the resolution tests using different node sizes and layer thicknesses (Figs 8 and 9, Figs S3–S5, Supporting Informatin), we observe that the horizontal spatial resolution of our model achieves approximately 7.5 km at a depth of 1.0 km and degrades to approximately 15.00 km at 7.0 km depth. Moreover, in the vertical direction, the model with increasing thickness shows better recovery than the one with relatively uniform thickness. However, due to the distribution of our array, the spatial resolution of our model is poorer at depths greater than 5 km between two corners of the array (around stations 1100 and 1162) compared to other parts of the array. This is primarily due to the reduced coverage of ray paths at longer periods beneath these stations (as shown in Figs 6g and h).

6.3 *S*-wave velocity results

In the inversion, considering the trade-off between the resolution and computation efficiency, a grid size of $0.030^\circ \times 0.034^\circ$ in the horizontal direction and a 1-D model with increasing layer thickness in the depth direction (mod2 in Fig. 7d) are chosen to establish the initial 3-D inversion model. We tested the number of iterations required for the inversion to achieve stable and reliable results, as shown in Fig. 10(a). After eight iterations, the RMS of the traveltime residuals began to stabilize. We ultimately chose to perform

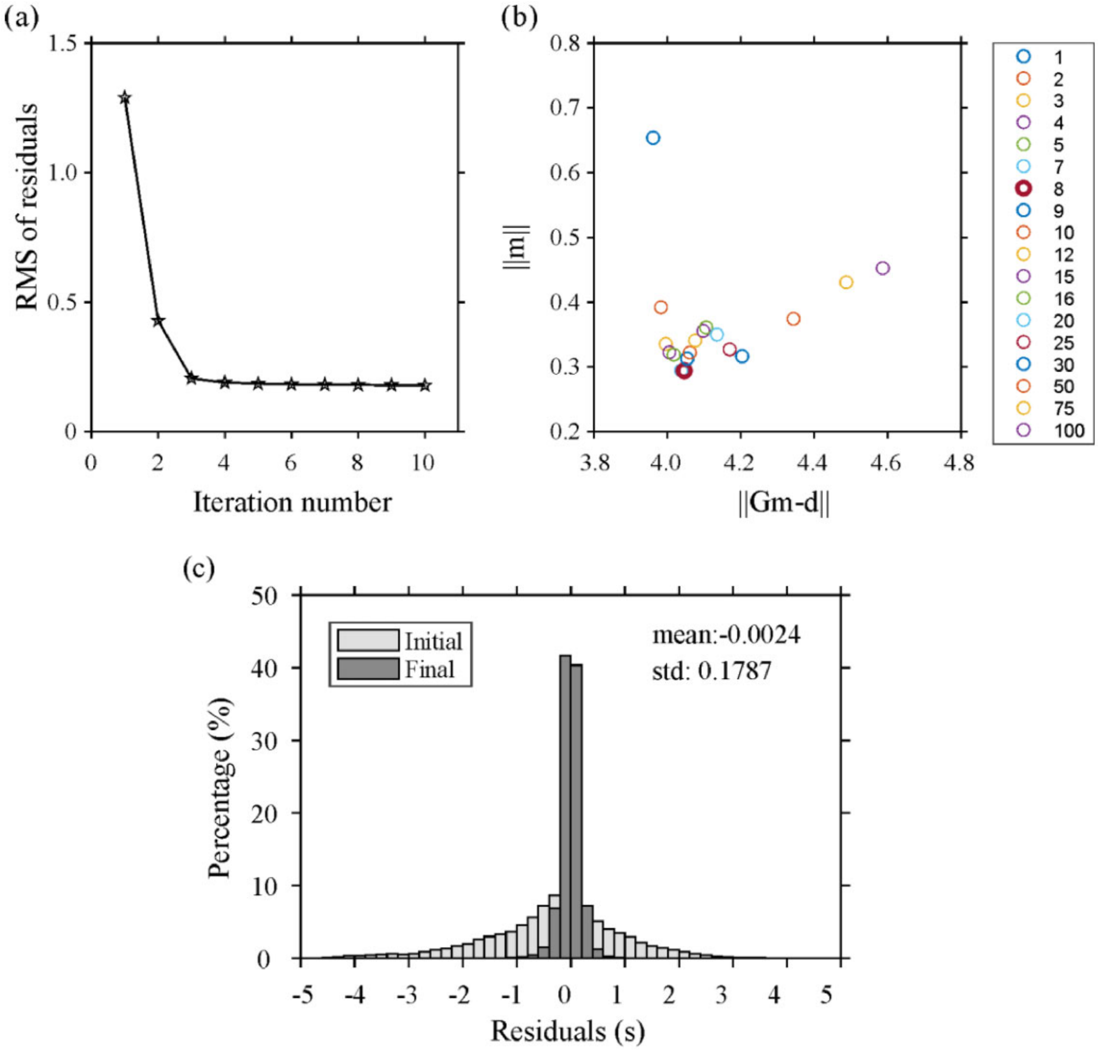

Figure 10. Tests for the inversion parameters. Determination of the iteration times (a) in the inversion process and the weight parameter (b) using the L-curve method. (c) Distribution of traveltime residuals before (in light grey) and after (in black) inversion. After the inversion, the mean of traveltime residuals decreases significantly from −0.2932 to −0.0024 s, and the standard deviation of traveltime residuals decreases from 1.2558 to 0.1787 s.

10 iterations, as this provided slightly better convergence of the RMS of the traveltime residuals compared to eight iterations. Another important parameter, the weight parameter, which balances the traveltime residuals and model smoothness, is also determined via a series of inversions with different parameters. According to the corner value of the L-curve shown in Fig. 10(b), we take the weight parameter of eight as the optimal parameter. Actually, the velocity profiles based on different weight parameters around the corner display minor differences, such as another two examples of velocity profiles obtained with lower (5) and higher (15) weight parameters in Figs 11(c) and (d).

After the inversion, we compute and compare the traveltime residuals at all periods before and after the inversion (Fig. 10c). The standard deviations of traveltime residuals at all periods after the inversion decrease from 1.2558 to 0.1787 s with almost zero means, indicating the final velocity model fits the dispersion data very well.

To further test the uncertainties of the resulting velocity models, we adopt the bootstrapping strategy to estimate standard errors of the inversion results. By generating 100 bootstrap samples from all the phase velocity measurements, each of the same size as the original data set through resampling with replacement, we perform inversion for each bootstrap sample. We then compute the average and standard error of the 100 inversion profiles (Figs 11e and f). The average velocity profile exhibits similar patterns to the final inversion results (Fig. 12b), with a minor standard error of less than 0.025 km s^{-1}.

The final V_{sh} profile at depths up to 10 km is plotted in Fig. 12(b) along the projection line shown in Fig. 1(b), which begins from the first station in the north to the last station in the south side. For more details, we also present various depth slices in Fig. S6 (Supporting Information). The V_{sh} model reveals a layered structure with low velocities ($< \sim$1.35 km s^{-1}) at very shallow depths and a quick velocity increase to high velocities of $>$ 3.25 km s^{-1} at greater depths. Since surface waves are sensitive to shear wave velocities over a range of depths, the V_{sh} model cannot accurately image the velocity boundary between the sediments and the basement (Li *et al.* 2019, 2021; Yang *et al.* 2023).

Considering that the sedimentary interfaces are typically associated with significant velocity changes, (Liu *et al.* 2012, 2016;

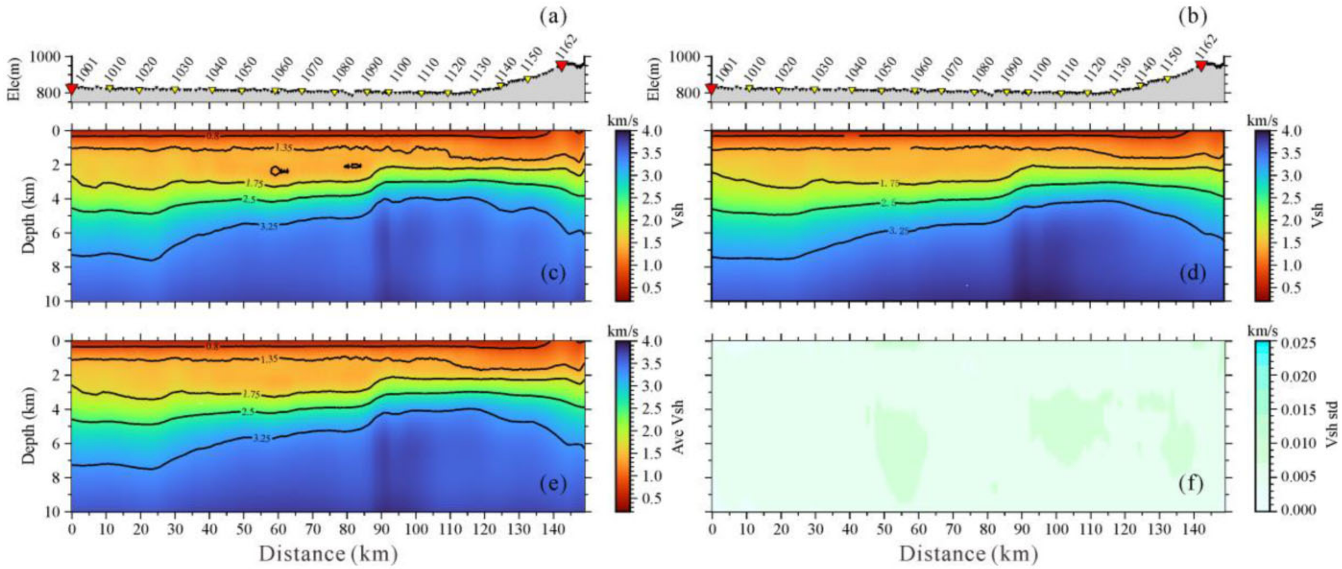

Figure 11 Tests of inversions for the V_{sh} velocity profiles using different weight parameters and data sets with bootstrapping strategy. (a) and (b) Topography beneath the deployed stations with an interval of 20 stations plotted on the top. (c) and (d) The V_{sh} velocity profiles obtained by inversions using different weight parameters around the corner of the L-curve in Fig. 10(b), with a smaller weight parameter of 5 in (c) and a larger weight parameter of 15 in (d). (e) and (f) The average V_{sh} velocity profile in (e) and estimations of uncertainties of V_{sh} velocity profiles in (f) obtained by bootstrapping strategy via generating 100 bootstrap samples from all the phase velocity measurements.

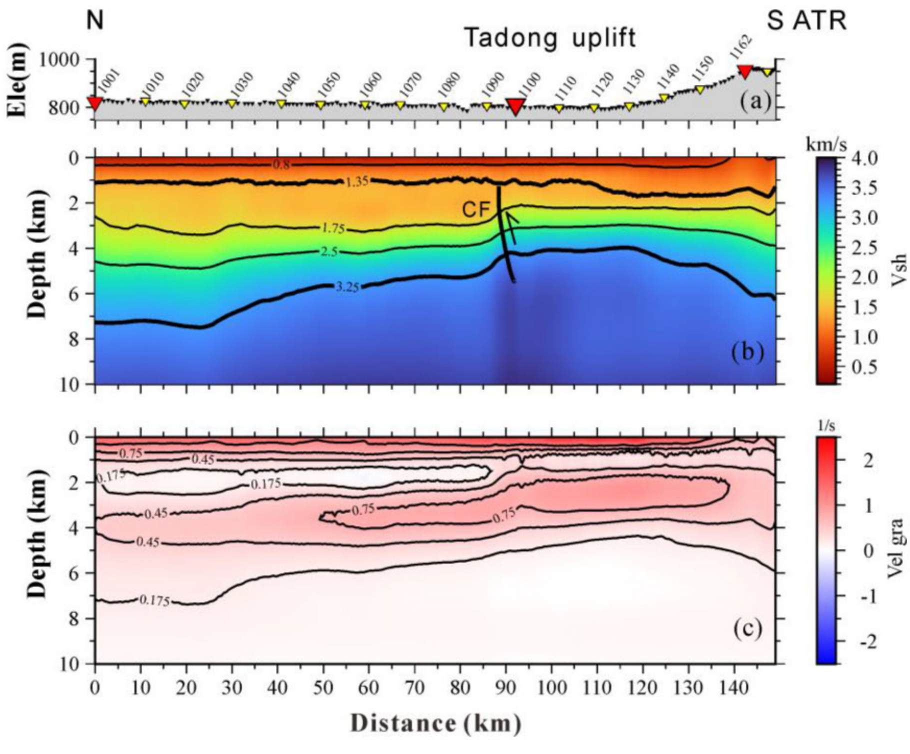

Figure 12. Final V_{sh} velocity profile. (a) Topography beneath the deployed stations with an interval of 20 stations plotted on the top. (b) V_{sh} profile along the projection line beginning from station 1001 to 1062, shown in Fig. 1. The solid black line of velocity $\sim$1.35 km s^{-1} is interpreted as the base of Paleogene sediments. The solid black line of velocity $\sim$3.25 km s^{-1} is interpreted as the base of the Sinian sediments above the deep crystalline basement. The solid black line with an arrow beneath station 1100 indicates the high-dipping CF with a steep ramp. (c) Vertical gradients of the above V_{sh} profile (b).

Molinari *et al.* 2015; Li *et al.* 2019, 2021; Wang *et al.* 2021, 2022), we here also calculate the velocity gradient showing the rate of velocity change in the vertical direction (Fig. 12c) to aid in identifying the positions of different geological boundaries and understanding the distribution and thickness of sedimentary layers as discussed in the following section.

7. DISCUSSIONS

To better understand the sedimentary structure and tectonic process at the southeast margin of the Tarim Basin, we combine our V_{sh} results with the results from receiver functions (Wu *et al.* 2024), balanced geological transects (Jiang *et al.* 2018; Laborde *et al.*

2019), active-source seismic profiles (Liu *et al.* 2012, 2016; Lin *et al.* 2012a; Jiang *et al.* 2018; Ren *et al.* 2018; Laborde *et al.* 2019) and drilling data (Yang *et al.* 2014; Yan *et al.* 2022). Based on the comparison, we discuss the structural characteristics of the southeast edge of the Tarim Basin in detail below.

First, we infer that sedimentary layers divided by two velocity boundaries may be formed during different geological periods, which are both indicated by significant velocity gradient changes from a relatively large velocity gradient (∼ 0.45) to a small value (∼ 0.175). The shallowest sedimentary layer with a low velocity of less than ∼1.35 km s^{-1} thickens from north to south and was likely formed from the Paleogene to the Quaternary as supported by the balanced geological transects and active-source seismic profiles (Lin *et al.* 2012a; Jiang *et al.* 2018; Laborde *et al.* 2019). The layer of the highest velocities (∼3.25 km s^{-1}) likely represents the base of the Sinian sediments above the deep crystalline basement, as also shown in the prospecting active-source reflection profile (Lin *et al.* 2012a; Ren *et al.* 2018; Laborde *et al.* 2019). This result is also in accordance with receiver function results in Wu *et al.* (2024) that show signals with positive conversions at depths of 6–9 km (red dashed line in Fig. S7, Supporting Information), suggesting the possible boundaries at these depths between the sedimentary layers and the underlying crystalline basement.

Secondly, we recognize an uplift with the high velocities (> ∼3.25 km s^{-1}) reaching a ∼4 km depth associated with the Tadong uplift, an important palaeo uplift in the Tarim Basin. Adjacent to and above the velocity uplift, a high-velocity gradient change of ∼ 0.75 also indicates the probable deformation of shallow sedimentary layers above the uplift. This uplift is also revealed by strong reflection phases in several active-source reflection profiles (Liu *et al.* 2012, 2016; Lin *et al.* 2012a; Laborde *et al.* 2019). Besides, a recent receiver function study by Wu *et al.* (2024) also shows a positive conversion signal CB1 from a boundary at ∼6–9 km depths interpreted as the Tadong uplift. The well loggings of TD1, TD2, DT1 and YD2 wells, located on the Tadong uplift, show that the distributions of the Sinian dolomite or the Proterozoic granite are present at ∼5 km depths (Yang *et al.* 2014; Yan *et al.* 2022). Previous geological analysis on the evolution of palaeo-uplifts in the basin indicates that the strongest deformation of the Tadong uplift is caused by the deformation occurring at the end of the Middle Devonian. This geological event is believed to be related to the subduction and collision between the Tianshan orogenic belt and the Altyn trench-arc-basin system (Lin *et al.* 2012b).

Thirdly, our model observes a lateral velocity jump near station 1100 associated with the high-dipping CF. Our results suggest that the CF is thrusting northward with a steep ramp, apparent both in the velocity profile and the corresponding velocity gradient profile (Fig. 12). Combined with the velocity discontinuities of this fault revealed by seismic profiles (Xu *et al.* 2009; Lin *et al.* 2012a, b; Laborde *et al.* 2019) (Fig. S8, Supporting Information), we consider the CF probably developed by cutting through the basement and the uplift on the hanging wall of this fault is up to ∼2 km. Studies on fault systems of the Tarim Basin also demonstrate that the CF is a large-scale basement fault and governs the distribution of first-grade geological units in this basin (Tang *et al.* 2014).

Lastly, our model is a V_{sh} velocity model, which may differ from isotropic V_s due to potential radial anisotropy in the sedimentary basin. Radial anisotropy, defined as the difference between V_{sv} and V_{sh}, can only be accurately determined by jointly inverting both Rayleigh and Love waves. Unfortunately, in this study, extracting dispersion curves of the longer period Rayleigh waves between individual station pairs is not feasible, unlike for Love waves, preventing us from performing a joint inversion. Therefore, estimating radial anisotropy in this area is challenging. However, employing subarray-based methods, for example, the F-J method, allows us to derive average multimode Rayleigh and Love wave dispersion curves from numerous CCFs obtained from a subarray (e.g. Fig. 4 and Fig. S2, Supporting Information). This approach presents a promising opportunity to investigate potential radial anisotropy in this area in our upcoming work.

8. CONCLUSIONS

In this study, we image the sedimentary structure of the southeast margin of the Tarim Basin from the surface to a 10 km depth using an environmentally friendly ambient noise tomography method. Applying ambient noise tomography to a dense short-period array, we construct a V_{sh} profile using dispersion curves of Love waves at a period band of ∼0.3–11.5 s. Our results reveal a clear layered sedimentary structure, pronounced characteristics of the palaeo Tadong uplift, and velocity discontinuities associated with the thrust CF. Our study provides a reference sedimentary velocity model for the southeastern Tarim Basin, specifically targeting shallow depths of less than 10 km. This model is expected to be an essential input for studies that necessitate detailed shallow sedimentary velocities. Furthermore, our work demonstrates that the dense array-based ambient noise tomography method can image the shallow sedimentary velocity structure for inland basins and can be applied to preliminary explorations of natural resources in thick sedimentary basins in the future.

ACKNOWLEDGMENTS

We thank editor Dr Paula Koelemeijer and the two anonymous reviewers for their valuable suggestions to improve our work. We are grateful for the fieldwork of data acquisition carried out by the Geophysical Exploration Center, China Earthquake Administration. We also thank Prof. Haibing Li for providing the figure for seismic reflection profiles and providing precious suggestions. We appreciate the constructive discussions and suggestions with Drs Youshan Liu, Jinyun Xie, Nanqiao Du, Wentao Li and Zimu Wu. Our work is financially supported by the Second Tibetan Plateau Scientific Expedition and Research Program (STEP) (2019QZKK0701-02) and the National Natural Science Foundation of China (Grant Numbers 42030308, 42130807 and 42104102).

SUPPORTING INFORMATION

Supplementary data are available at *GJIRAS* online.

Figure S1. Examples of *ZZ* component CCFs.
Figure S2. Similar to Fig. 4, but for the *RR* component.
Figure S3. Similar to Figs 8 and 9, but for resolution tests with grid node sizes of 0.015° × 0.017°.
Figure S4. Similar to Figs 8 and 9, but for resolution tests with grid node sizes of 0.020° × 0.020°.
Figure S5. Similar to Figs 8 and 9, but for resolution tests with grid node sizes of 0.040° × 0.040°.
Figure S6. Shear wave velocity slices at different depths.
Figure S7. Comparison with the results from receiver functions in Wu *et al.* (2024).

Figure S8. Comparison with previous active seismic profiles and wells.

Please note: Oxford University Press is not responsible for the content or functionality of any supporting materials supplied by the authors. Any queries (other than missing material) should be directed to the corresponding author for the paper.

DECLARATION OF COMPETING INTERESTS

All the authors of this paper declare that there are no conflicts of interest recorded.

DATA AVAILABILITY

The dispersion curves of the Love wave and V_{sh} velocity models at each station in this paper can be accessed from the online repository (https://doi.org/10.6084/m9.figshare.26196119.v1). The codes of the DSurfTomo method are open source and can be obtained on the website: https://github.com/HongjianFang/DSurfTomo (last accessed on 2024 January 9). More information and the open-source codes of CPS can be obtained on the website: https://doi.org/10.1785/0220110096 (last accessed on October 4, 2024).

REFERENCES

Bao, F., Li, Z., Yuen, D.A., Zhao, J., Ren, J., Tian, B. & Meng, Q., 2018. Shallow structure of the Tangshan fault zone unveiled by dense seismic array and horizontal-to-vertical spectral ratio method, *Phys. Earth planet. Inter.,* **281,** 46–54.

Bensen, G.D., Ritzwoller, M.H., Barmin, M.P., Levshin, A.L., Lin, F.-C., Moschetti, M.P., Shapiro, N.M. & Yang, Y., 2007. Processing seismic ambient noise data to obtain reliable broad-band surface wave dispersion measurements, *Geophys. J. Int.,* **169**(3), 1239–1260.

Chmiel, M. *et al.*, 2019. Ambient noise multimode Rayleigh and Love wave tomography to determine the shear velocity structure above the Groningen gas field, *Geophys. J. Int.,* **218**(3), 1781–1795.

Corela, C., Silveira, G., Matias, L., Schimmel, M. & Geissler, W.H., 2017. Ambient seismic noise tomography of SW Iberia integrating seafloor- and land-based data, *Tectonophysics,* **700-701,** 131–149.

Fang, H., Yao, H., Zhang, H., Huang, Y.-C. & van der Hilst, R.D., 2015. Direct inversion of surface wave dispersion for three-dimensional shallow crustal structure based on ray tracing: methodology and application, *Geophys. J. Int.,* **201**(3), 1251–1263.

Herrmann, R.B., 2013. Computer programs in seismology: an evolving tool for instruction and research, *Seismol. Res. Lett.,* **84**(6), 1081–1088.

Hu, S., Luo, S. & Yao, H., 2020. The frequency-bessel spectrograms of multicomponent cross-correlation functions from seismic ambient noise, *J. geophys. Res. Solid Earth,* **125**(8), e2020JB019630, doi:10.1029/2020JB019630.

Huang, S. *et al.*, 2017. Types and characteristics of carbonate reservoirs and their implication on hydrocarbon exploration: a case study from the eastern Tarim Basin, NW China, *J. Nat. Gas Geosci.,* **2**(1), 73–79.

Jiang, C. & Denolle, M.A., 2022. Pronounced seismic anisotropy in Kanto Sedimentary Basin: a case study of using dense arrays, ambient noise seismology, and multi-modal surface-wave imaging, *J. geophys. Res. Solid Earth,* **127**(8), e2022JB024613, doi:10.1029/2022JB024613.

Jiang, Z., Jiang, S., Lan, X., Wang, B., Huang, S. & Zhang, H., 2018. Neotectonic evolution of the Tarim Basin Craton from neogene to quaternary, *Int. Geol. Rev.,* **60**(10), 1213–1230.

Kang, Y., 2018. The resource potential and exploration for oil and gas in the Tarim Basin, *Pet. Sci.Bull.,* **3**(4), 369–375 (in Chinese).

Laborde, A., Barrier, L., Simoes, M., Li, H., Coudroy, T., Van der Woerd, J. & Tapponnier, P., 2019. Cenozoic deformation of the Tarim Basin and surrounding ranges (Xinjiang, China): a regional overview, *Earth Sci. Rev.,* **197,** 102891, doi:10.1016/j.earscirev.2019.102891.

Levshin, A.L. & Ritzwoller, M.H.(2001). Automated detection, extraction, and measurement of regional surface waves, *Pure appl. Geophys.,* **158,** 1531–1545.

Li, G., Chen, H., Niu, F., Guo, Z., Yang, Y. & Xie, J., 2016. Measurement of Rayleigh wave ellipticity and its application to the joint inversion of high-resolution S wave velocity structure beneath northeast China, *J. geophys. Res. Solid Earth,* **121**(2), 864–880.

Li, G., Niu, F., Yang, Y. & Tao, K., 2019. Joint inversion of Rayleigh wave phase velocity, particle motion, and teleseismic body wave data for sedimentary structures, *Geophys. Res. Lett.,* **46**(12), 6469–6478.

Li, G., Yang, Y., Niu, F. & Chen, M., 2021. 3-D sedimentary structures beneath southeastern Australia constrained by passive seismic array data, *J. geophys. Res. Solid Earth,* **126**(2), e2020JB019998, doi:10.1029/2020JB019998.

Li, H., Li, S., Song, X.D., Gong, M., Li, X. & Jia, J., 2012. Crustal and uppermost mantle velocity structure beneath northwestern China from seismic ambient noise tomography, *Geophys. J. Int.,* **188**(1), 131–143.

Lin, C., Yang, H., Liu, J., Rui, Z., Cai, Z., Li, S. & Yu, B., 2012a. Sequence architecture and depositional evolution of the ordovician carbonate platform margins in the Tarim Basin and its response to tectonism and sea-level change, *Basin Res.,* **24**(5), 559–582.

Lin, C., Yang, H., Liu, J., Rui, Z., Cai, Z. & Zhu, Y., 2012b. Distribution and erosion of the paleozoic tectonic unconformities in the Tarim Basin, Northwest China: significance for the evolution of paleo-uplifts and tectonic geography during deformation, *J. Asian Earth Sci.,* **46,** 1–19.

Lin, F.-C., Li, D., Clayton, R.W. & Hollis, D., 2013. High-resolution 3D shallow crustal structure in Long Beach, California: application of ambient noise tomography on a dense seismic arrayNoise tomography with a dense array, *Geophysics,* **78**(4), Q45–Q56.

Lin, F.-C., Moschetti, M.P. & Ritzwoller, M.H., 2008. Surface wave tomography of the western United States from ambient seismic noise: rayleigh and Love wave phase velocity maps, *Geophys. J. Int.,* **173**(1), 281–298.

Lin, F.-C., Tsai, V.C. & Schmandt, B., 2014. 3-D crustal structure of the western United States: application of Rayleigh-wave ellipticity extracted from noise cross-correlations, *Geophys. J. Int.,* **198**(2), 656–670.

Liu, H., Lin, C., Wang, Y. & Zhang, D., 2012. Temporal and spatial evolution analysis: the early paleozoic paleo-uplifts in the Tarim basin, *J. Earth Sci.,* **23**(4), 559–581.

Liu, H., Somerville, I.D., Lin, C. & Zuo, S., 2016. Distribution of palaeozoic tectonic superimposed unconformities in the Tarim Basin, NW China: significance for the evolution of palaeogeomorphology and sedimentary response, *Geol. J.,* **51**(4), 627–651.

Lü, Z., Gao, H., Lei, J., Yang, X., Rathnayaka, S. & Li, C., 2019. Crustal and upper mantle structure of the Tien Shan orogenic belt from full-wave ambient noise tomography, *J. geophys. Res. Solid Earth,* **124**(4), 3987–4000.

Molinari, I., Argnani, A., Morelli, A. & Basini, P., 2015. Development and testing of a 3D seismic velocity model of the Po Plain sedimentary basin, Italy, *Bull. seism. Soc. Am.,* **105**(2A), 753–764.

Rawlinson, N. & Sambridge, M., 2005. The fast marching method: an effective tool for tomographic imaging and tracking multiple phases in complex layered media, *Explor. Geophys.,* **36**(4), 341–350.

Ren, R., Guan, S., Wu, L. & Zhu, G., 2018. Evolution of the neoproterozoic rift basins and its implication for oil and gas exploration in the Tarim Basin, *Pet. Res.,* **3**(1), 66–76.

Rivet, D., Campillo, M., Sanchez-Sesma, F., Shapiro, N.M. & Singh, S.K., 2015. Identification of surface wave higher modes using a methodology based on seismic noise and coda waves, *Geophys. J. Int.,* **203**(2), 856–868.

Sabra, K.G., Gerstoft, P., Roux, P., Kuperman, W. & Fehler, M.C., 2005. Extracting time-domain Green's function estimates from ambient seismic noise, *Geophys. Res. Lett.,* **32**(3), doi:10.1029/2004GL021862.

Sun, W., Ao, S., Tang, Q., Malusà, M.G., Zhao, L. & Xiao, W., 2022. Forced cenozoic continental subduction of Tarim craton-like lithosphere below the Tianshan revealed by ambient noise tomography, *Geology,* **50**(12), 1393–1397.

Tan, P., Liang, X., Li, W. & Wu, C., 2023. Crustal structure of the Tibetan Plateau and adjacent areas revealed from ambient noise tomography, *Gondwana Res.,* **121,** 1–15.

Tang, L., Huang, T., Qiu, H., Wan, G., Li, M., Yang, Y., Xie, D. & Chen, G., 2014. Fault systems and their mechanisms of the formation and distribution of the Tarim Basin, NW China, *J. Earth Sci.,* **25,** 169–182.

Tian, J., Wang, Q., Yang, H. & Li, Y., 2021. Petroleum exploration history and enlightenment in Tarim Basin, *Xinjiang Pet. Geol.,* **42**(3), 272–282 (in Chinese).

Tomar, G., Stutzmann, E., Mordret, A., Montagner, J.-P., Singh, S.C. & Shapiro, N.M., 2018. Joint inversion of the first overtone and fundamental mode for deep imaging at the Valhall oil field using ambient noise, *Geophys. J. Int.,* **214**(1), 122–132.

Viens, L., Koketsu, K., Miyake, H., Sakai, S.i. & Nakagawa, S., 2016. Basin-scale Green's functions from the ambient seismic field recorded by MeSO-net stations, *J. geophys. Res. Solid Earth,* **121**(4), 2507–2520.

Wang, J., Wu, G. & Chen, X., 2019a. Frequency-bessel transform method for effective imaging of higher-mode rayleigh dispersion curves from ambient seismic noise data, *J. geophys. Res. Solid Earth,* **124**(4), 3708–3723.

Wang, X. *et al.*, 2022. Shallow crustal response to Arabia-Eurasia convergence in northwestern Iran: constraints from multifrequency P-wave receiver functions, *J. geophys. Res. Solid Earth,* **127**(9), e2022JB024515, doi:10.1029/2022JB024515.

Wang, X., Chen, L. & Yao, H., 2021. A new body-wave amplitude ratio-based method for imaging shallow crustal structure and its application in the Sichuan Basin, Southwestern China, *Geophys. Res. Lett.,* **48**(18), e2021GL095186, doi:10.1029/2021GL095186.

Wang, Y., Allam, A. & Lin, F.-C., 2019b. Imaging the Fault damage zone of the San Jacinto Fault near Anza with ambient noise tomography using a dense nodal array, *Geophys. Res. Lett.,* **46**(22), 12938–12948.

Wu, C., Xu, T., Tian, X., Mitchell, R.N., Lin, J., Yang, J., Wang, X. & Lu, Z., 2024. Underthrusting of Tarim lower crust beneath the Tibetan plateau revealed by receiver function imaging, *Geophys. Res. Lett,* **51,** e2024GL108220, doi:10.1029/2024GL108220.

Xie, J., Luo, Y., Yang, Y., Xie, Y. & Yang, X., 2023a. On the accuracy of surface-wave dispersion measurements from horizontal-component ambient noise cross correlations, *Seismol. Res. Lett.,* **94**(6), 2787–2800.

Xie, T., Xu, T., Yang, Y., Tian, X., Lin, J., Wu, C. & Lu, Z., 2023b. Observation of higher-mode rayleigh waves from ambient noise in the Tarim Basin, China, *Seismol. Res. Lett.,* **94**(4), 1848–1859.

Xu, H., Zhang, Y., Liu, X., Zhou, C. & Xu, J., 2009. Sedimentary-structural characteristics and tectonic evo;ution history of the Tadongnan Uplift, *Geol. China,* **36,** 1030–1045. http://geochina.cgs.gov.cn/en/article/id/20090508 (in Chinese)

Yan, L., Wei, G., Zhu, G., Chen, Y., Luo, C., Yang, M., Wang, S. & Du, D., 2022. Exploration field analysis and zone optimization of sinian, Tarim Basin, China, *J. Nat. Gas Geosci.,* **7**(3), 171–179.

Yang, X. *et al.* 2021. Geological understanding and favorable exploration fields of ultra-deep formations in Tarim Basin, *China Pet. Explor.,* **26**(4), 17–28 (in Chinese).

Yang, X., Luo, Y., Jiang, C., Yang, Y., Niu, F. & Li, G., 2023. Crustal and upper mantle velocity structure of SE Tibet from joint inversion of Rayleigh wave phase velocity and teleseismic body wave data, *J. geophys. Res. Solid Earth,* **128**(7), e2022JB026162, doi:10.1029/2022JB026162.

Yang, X., Xu, X., Qian, Y., Chen, Q., Chu, C. & Jiang, H., 2014. Discussion on regional differences in basement composition of the Tarim Basin, *Geotect. Metall.,* **38,** 544–556. https://link.cnki.net/doi/10.16539/j.ddgzyckx.2014.03.004 (in Chinese).

Yang, Y. *et al.* 2010. Rayleigh wave phase velocity maps of Tibet and the surrounding regions from ambient seismic noise tomography, *Geochem. Geophys. Geosyst.,* **11**(8), doi:10.1029/2010GC003119.

Yang, Y., Ritzwoller, M.H., Levshin, A.L. & Shapiro, N.M., 2007. Ambient noise Rayleigh wave tomography across Europe, *Geophys. J. Int.,* **168**(1), 259–274.

Yao, H., van Der Hilst, R.D. & De Hoop, M.V., 2006. Surface-wave array tomography in SE Tibet from ambient seismic noise and two-station analysis—I. Phase velocity maps, *Geophys. J. Int.,* **166**(2), 732–744.

Yao, S., Xu, T., Sang, Y., Ye, L., Yang, T., Wu, C. & Zhang, M., 2024. The seismicity in the middle section of the Altyn Tagh Fault system revealed by a dense nodal seismic array, *Earthq. Res. Adv.,* **4,** 100308, doi:10.1016/j.eqrea.2024.100308.

Zhao, J., Mooney, W.D., Zhang, X., Li, Z., Jin, Z. & Okaya, N., 2006. Crustal structure across the Altyn Tagh Range at the northern margin of the Tibetan Plateau and tectonic implications, *Earth planet. Sci. Lett.,* **241**(3–4), 804–814.

Zhao, K., Yang, Y. & Luo, Y., 2020. Broadband finite frequency ambient noise tomography: a case study in the western United States using USArray stations, *J. geophys. Res. Solid Earth,* **125**(6), e2019JB019314, doi:10.1029/2019JB019314.